ACS Partner Journal

Journal of the American Society for Mass Spectrometry

pubs.acs.org/jasms

Article

Impact of Charge State on Characterization of Large Middle-Down Sized Peptides by Tandem Mass Spectrometry

Jessica Hellinger and Jennifer S. Brodbelt*

Cite This: *J. Am. Soc. Mass Spectrom.* 2024, 35, 1647−1656

Read Online

ACCESS | Metrics & More | Article Recommendations | Supporting Information

ABSTRACT: Fragmentation trends of large peptides were characterized by five activation methods, including HCD, ETD, EThcD, 213 nm UVPD, and 193 nm UVPD. Sequence coverages and scores were assessed based on charge site, peptide sequence, and peptide size. The effect of charge state and peptide size on sequence coverage was explored for a Glu-C digest of *E. coli* ribosomal proteins, and linear regression analysis of the collection of peptides indicated that HCD, ETD, and EThcD have a higher dependence charge state than 193 and 213 nm UV. Four model peptides, neuromedin, glucagon, galanin, and amyloid β, were characterized in greater detail based on charge site analysis and showed a charge state dependence on sequence coverage for collision and electron-based activation methods.

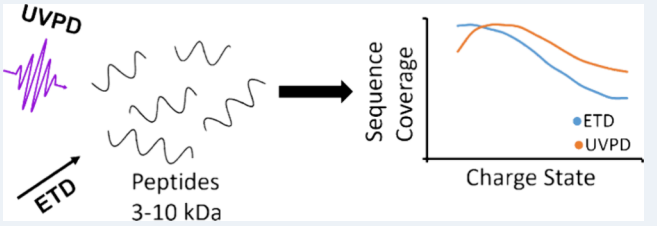

INTRODUCTION

Owing to the complexity of the proteome and its vast implications on understanding human health and disease, numerous high throughput liquid chromatography−mass spectrometry (LC−MS) methods have been developed for protein identification, quantification, localization of post-translational modifications (PTM), and characterization of combinatorial effects of such modifications on protein structure and function.[1] These methods typically fall into two categories, top-down strategies, which involve the analysis of intact proteins, and bottom-up approaches, which entail the analysis of small peptides generated from proteolysis of proteins. Middle-down proteomics is an intermediate between top-down and bottom-up methods, focusing on the analysis of large peptides in a manner that combines many of the strengths and overcoming some of the limitations of the other two methods.[2] Middle-down proteomic workflows involve partial digestion of proteins, using proteases such as GluC, AspN, LysC,[3−6] or through chemical digestion,[7] which leads to peptides between 3−7 kDa. Other highly specific proteases, IdeS and IdeZ, cleave antibodies at unique positions and generate large subunits.[8−10] By comparison, proteases used for bottom-up workflows typically result in peptide sizes less than 3 kDa. Due to the larger peptides produced using middle-down methods, each peptide has the potential to afford more sequence information and has a greater likelihood of containing multiple PTMs, thus increasing the opportunity to identify and map combinatorial modifications.[11−13] The ability of middle-down methods to map combinatorial modifications is especially important for applications involving highly modified proteins that code information for protein function and signal transduction.[14] Analysis of intact proteins using top-down workflows circumvents most concerns about retaining the context of all PTMs.[15] However, technical challenges related to chromatographic separation efficiencies and low sequence coverages afforded by MS/MS methods have motivated ongoing efforts to improve middle-down approaches.

Regardless of the category of proteomics strategy (bottom-up, middle-down, or top-down), identifying the peptides or proteins of interest depends on proficient MS/MS methods that enable sufficient fragmentation to decipher the sequences, and both localize and characterize PTMs. Fragmentation trends vary with the size, charge state, and amino acid composition of each peptide or protein as well as the ion activation method. One concept used to rationalize the fragmentation of peptides and proteins produced by collision induced dissociation (CID) is the mobile proton model, initially developed to explain the variations in fragmentation of peptides as a function of charge state.[16] For peptides in low charge states, all protons are sequestered at basic sites, such as arginine and lysine, and this results in charge-remote fragmentation pathways that favor production of preferential backbone cleavages C-terminal to acidic residues. As the charge state increases and the number of protons exceeds the number of basic sites, protons can migrate to other sites through intramolecular proton transfer reactions. This mobility of protons promotes charge-directed fragmentation pathways

Received: November 21, 2023
Revised: May 14, 2024
Accepted: July 2, 2024
Published: July 16, 2024

that result in a greater range of backbone cleavages throughout the peptide or protein, including significantly enhanced cleavages N-terminal to proline residues. The mobile proton model explains the higher energies required to fragment peptides in low charge states as well as the shift in fragmentation pathways of peptides from neutral losses and preferential cleavages adjacent to acidic residues for low charge states to a broader array of backbone cleavages for high charge states.[16,17] The fragmentation efficiency of electron-based activation methods (electron transfer dissociation (ETD) and electron capture dissociation (ECD)) has also been linked to charge state (or more accurately, "charge density"), with more effective fragmentation occurring for higher charge states owing to greater cation recombination energies that result in more exothermic electron transfer reactions.[18] Ultraviolet photodissociation (UVPD) is another ion activation method that typically results in the greatest array of fragment ion types.[19] The process of ultraviolet photodissociation (UVPD) entails excitation of ions to excited electronic states and direct fragmentation to produce *a*/*x*-type ions or internal conversion and intramolecular vibrational energy redistribution prior to fragmentation.[20] The impact of charge state and location of charges of peptides and proteins has been evaluated using UVPD.[21−24]

All of these ion activation methods have been applied for middle-down proteomics. For example, analysis of middle-down sized peptides has been explored using CID,[25] ETD and EThcD,[26,27] and UVPD using both 193 nm[8,28,29] and 213 nm[30] photons. Both UVPD[28,29] and electron-based methods[10,31] have generally surpassed the performance of collisional activation methods for comprehensive analysis of large peptides and localization of modifications, although the benefits of combining multiple fragmentation types is widely acknowledged.[8,30,32]

In this work, we investigate fragmentation trends for HCD, ETD, EThcD, 193 nm UVPD, and 213 nm UVPD for large middle-down sized peptides based on size and charge states. A GluC digest of ribosomal proteins from *E. coli* is used to optimize sequence coverage for an array of larger peptides. Linear regression is used to dissect scatter plots that examine sequence coverage vs peptide mass or peptide charge state for the collection of identified peptides. The impact of the number of basic sites, derived based on an estimation of the number of mobile proteins relative to charge state, on trends in sequence coverage and performance of the five ion activation methods is explored. We also characterize four model peptides ranging in size from 3−5 kDa and containing a number of basic residues (Arg, Lys) to correlate trends in fragmentation efficiencies of CID and UVPD with charge states, determine charge sites of the peptides based on charge state analysis of the fragment ions generated by UVPD, and compare the efficiencies of ETD and EThcD for analysis of large peptides.

MATERIAL AND METHODS

Chemicals. Neuromedin, glucagon, galanin, and amyloid β (1−40) were purchased from Cayman Chemicals (Ann Arbor, Michigan). All samples were prepared in 50/50 methanol/water with 0.1% formic acid, between 1 and 10 μM. *E. coli* ribosome and *Staphylococcus aureus* V8 endoproteinase Glu-C were purchased from New England Biolabs (Ipswich, MA).

Preparation of Ribosomal Protein Digest. Nucleic acids were removed from the *E. coli* ribosome by addition of 20 μL of 100 mM magnesium acetate and 80 μL glacial acetic acid to 50 μg of ribosome suspension. The solution was incubated at 4 °C for 1 h prior to centrifugation to pellet the RNA. The supernatant was removed and buffer exchanged into 50 mM ammonium bicarbonate and 8 M urea using a 3 kDa molecular weight cutoff filter. The disulfide bonds in the resulting mixture of ribosomal proteins were reduced with 5 mM dithiothreitol (DTT) for 30 min at 55 °C and alkylated with 15 mM iodoacetamide (IAM) for 30 min at room temperature in the dark. The solution was diluted by half with 50 mM ammonium bicarbonate. The ribosomal proteins were digested with GluC at a 1:100 enzyme to protein ratio at 37 °C overnight. The reaction was quenched with 0.1% formic acid and diluted with water to 500 μL prior to cleaning with a 3 kDa MWCO filter into a final solution composition of water with 0.1% formic acid prior to LC−MS analysis.

Mass Spectrometry. Mass spectra of neuromedin, glucagon, galanin, and amyloid β (1−40) were collected on a Thermo Orbitrap Fusion Lumos Tribrid mass spectrometer (Thermo Fisher, San Jose, CA), equipped with either a Coherent Excistar XS excimer laser (193 nm, 500 Hz, 5 ns pulse length) (as described previously)[33] or a solid state 213 nm laser (2500 Hz, 2 uJ per pulse) for UVPD. Peptides were introduced by nanoelectrospray ionization using an applied voltage of 1.2 kV. Borosilicate capillaries (OD: 1.2 mm, ID: 0.69 mm) were pulled in-house and coated with Au/Pd for use as static emitters for direct infusion. Spectra were collected at 120 k resolution with 100 averages. MS/MS spectra were collected with higher-energy collisional dissociation (HCD) collision energies between 5 and 40 NCE corresponding to 0−80 eV, and EThcD using a 50 ms reaction period with fluoranthene and 20 NCE. 193 nm UVPD spectra were collected using 1 pulse at 2 mJ. For 213 nm UVPD, a 100 ms activation period was used, equating to 250 laser pulses.

LC−MS. The *E. coli* ribosomal protein digest was analyzed using a Dionex RSLC 3000 nano-LC system (Thermo Fischer, San Jose, CA) interfaced to the mass spectrometer. 1 μL of the digest was injected per LC run. Peptides were eluted onto a 3 cm long polymer reversed-phase PLRP trap column (ID 100 μm, 5 μm particles, 1000 Å pore size, packed in-house) and 20 cm long PLRP analytical column (ID 75 μm, 1.8 μm particles, 1000 Å pore size, packed in-house). An 80 min linear gradient from 2% to 35% mobile phase B (acetonitrile with 0.1% formic acid) was used for separations, and water with 0.1% formic acid was used as mobile phase A. The separation was performed at a flow rate of 0.3 μL/min. The five most abundant ion peaks in each MS1 spectrum were selected for MS/MS analysis. For smaller peptides, often only a single charge state (e.g., 2+) was analyzed, whereas for the largest peptides, up to five charge states were selected. MS/MS spectra were collected with the same parameters as previously mentioned.

Data Analysis. Spectra from the peptides (neuromedin, glucagon, galanin, and amyloid-β) were deconvoluted with Xtract in FreeStyle with a S/N threshold of 3. Sequence coverage (based on the percentage of inter-residue cleavages per peptide) and fragmentation maps were generated using MS-TAFI[34] (an in-house program for UVPD spectral analysis). Charge state analysis was performed using UV-POSIT[35] based on analysis of the charge states of *a*-type fragment ions. Both MS-TAFI and UV-POSIT were analyzed with a 10 ppm tolerance and S/N cutoff of 3. To generate fragmentation efficiency curves, CID spectra were collected using collision energies ranging from 0 to 40 NCE at 5 NCE increments (0−80 eV). Spectra were deconvoluted using Xtract, and

https://doi.org/10.1021/jasms.3c00405
J. Am. Soc. Mass Spectrom. 2024, 35, 1647−1656

fragmentation efficiencies and fragmentation efficiency curves were generated based on the summed abundances of all identified and unidentified fragment ions divided by the total ion current (abundances of all identified and unidentified fragment ions plus abundance of the surviving precursor ion). Analysis of the *E. coli* ribosomal protein middle-down digest was performed using Proteome Discoverer (version 3.0) with a database of all *E. coli* proteins based on a GluC digestion. Scores are reported as −log(P-score) where a P-score closer to 0 indicates a good match and a P-score closer to 1 indicates a poor match. The score cutoff value was set to 20 (P-score 0.01). All data was collected with three replicates. Scatter plots created for the peptides from the GluC digest were subjected to linear regression analysis in Python based on sequence coverage vs peptide mass and sequence coverage vs peptide charge state. Linear regression analysis of the scatter plots was also further refined to categorize the peptides based on an estimation of the number of mobile proteins, (i.e., [charge state of peptide−number of basic amino acids]).

RESULTS AND DISCUSSION

Analysis of Large Peptides Produced from GluC Digestion of Ribosomal Proteins. An array of large peptides were generated based on a limited GluC digestion of the ribosomal proteins in *E. coli*, and these were analyzed via an LC−MS/MS workflow. GluC was chosen as the protease in order to target middle-down sized peptides. An exemplative chromatographic trace is shown in Figure S1. The sequence coverages and scores (e.g., −log(P-score)) were used to compare the performance of each activation method. Proteome Discoverer results are shown in Tables S1−5. Peptides with scores below 20, equivalent to a P-score of 0.01, were discarded. A total of 200 peptides were identified across all MS/MS methods, with 76 identified in common among all five activation methods, resulting in identification of 46 of the 54 proteins in the ribosomal complex. Among the five activation methods, HCD and EThcD identified the largest number of peptides (152 and 148, respectively), and the two UVPD methods identified fewer peptides (106 peptides for 213 nm UVPD and 107 peptides for 193 nm UVPD).

To facilitate comparison of the outcomes of the five activation methods, the number of peptides identified, average sequence coverages, and scores were assessed based on peptides grouped in 2 kDa bins (Figure 1). The differences in numbers of identified peptides primarily arise from the pool of peptides less than 2 kDa, for which an average of 42, 26, and 37 peptides were identified by HCD, ETD and EThcD, respectively. In comparison, an average of 8 peptides were identified by 193 nm UVPD and 10 peptides by 213 nm UVPD (Figure 1a) for these low mass bins. The peptides in this lower mass range are not the primary target of this middle-down study.

EThcD yielded the highest average sequence coverages for the lower mass peptides: 87% for peptides less than 2 kDa and 83% for peptides between 2 and 4 kDa. Sequence coverages for all five activation methods decreased for larger peptides; however, the sequence coverages obtained from UVPD surpassed EThcD for larger peptides (≥6 kDa). 193 nm UVPD afforded the highest average sequence coverages for peptides from 4 to 6 kDa (65%) and 6−8 kDa (57%), and both 193 and 213 nm UVPD returned equivalent sequence coverage for peptides from 8 to 10 kDa (53%) (Figure 1b). Only a single peptide was identified above 10 kDa, preventing

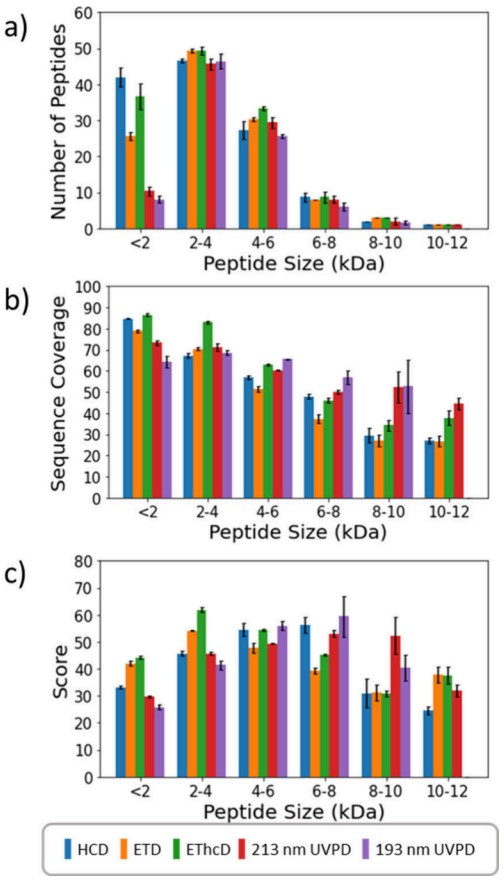

Figure 1. Average (a) number of peptides, (b) sequence coverage, and (c) scores (i.e. −log(P-score)) of Glu-C peptides from *E. coli* ribosomal proteins identified by HCD (152 peptides), ETD (125 peptides), EThcD (148 peptides), 213 nm UVPD (106 peptides), and 193 nm UVPD (107 peptides) grouped in 2 kDa bins.

meaningful comparisons. The scores reflect a similar trend as the sequence coverages, in which EThcD resulted in higher average scores for peptides less than 4 kDa and UVPD yielded higher scores for large peptides, specifically in the 8−10 kDa range, for which 193 and 213 nm UVPD gave average scores of 40 and 52, respectively, compared to HCD, ETD and EThcD, which yielded average scores of 31 (Figure 1c). The full data sets for sequence coverage and score are shown as scatter plots, which display the range of sequence coverages (Figure S2) and scores (Figure S3) for every identified peptide for each fragmentation method as a function of peptide mass. Maximum sequence coverages for peptides identified by HCD, ETD, and EThcD occurred in the 2−4 kDa range and in the 2−6 kDa range for 193 and 213 nm UVPD (Figure S2). The maximum scores occurred around 6 kDa for HCD, 3 kDa for ETD and EThcD, and between 4 and 6 kDa for 213 and 193 nm UVPD (Figure S3).

Trends in the average sequence coverages and scores as a function of peptide charge state are displayed in Figure S4. Average sequence coverages are highest for EThcD for peptides in the 3+ to 8+ charge states and are overtaken by 193 nm UVPD for peptides in the 9+ to 12+ charge states and 213 nm UVPD for peptides in the 13+ to 17+ charge states (Figure S4a). Average scores of peptides binned by charge state show similar trends: highest scores are generated by EThcD for the lowest charge states, 3+ to 6+, whereas UVPD yielded higher scores for the 7+ to 13+ charge states, and ETD

https://doi.org/10.1021/jasms.3c00405
J. Am. Soc. Mass Spectrom. 2024, 35, 1647−1656

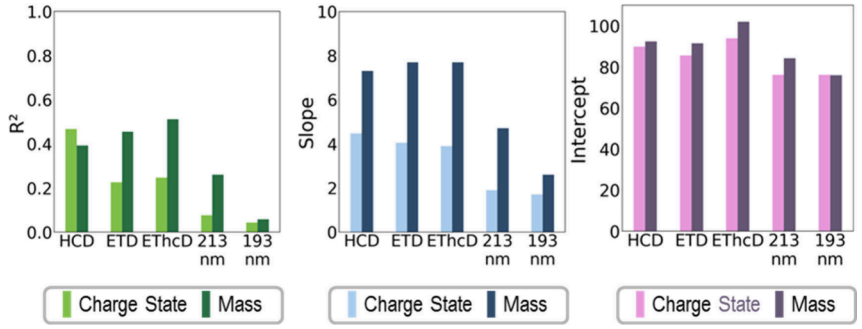

Figure 2. Correlation R^2 values, slopes, and intercepts of the linear regressions for the scatter plots of sequence coverage vs charge state and sequence coverage vs mass. Slopes for the sequence coverage vs mass were multiplied by −1000, and sequence coverage vs charge state by −1 in order to facilitate visualization.

and EThcD returned the greatest average scores for the highest charge states, 14+ to 19+ (Figure S4b).

Scatter plots of sequence coverage (Figure S5) and score (Figure S6) are shown for the full data sets as a function of charge state. Maximum sequence coverages of 100% are obtained for ETD of 3+ and 4+ peptides, whereas HCD affords maximum sequence coverage for peptides up to the 5+ charge state and EThcD up to the 7+ charge state. Greater than 90% sequence coverage is achieved for 193 and 213 nm UVPD for peptides in charge states ranging from 4+ to 8+ (Figure S5). In contrast to a range of charge states achieving high sequence coverage, scores appear to crest for a narrower range of charge states: 5+ for HCD and EThcD versus 5+ to 7+ for 193 and 213 nm UVPD (Figure S6). These trends are not unexpected because larger peptides typically yield higher charge state distributions, although some observed trends vary slightly based on peptide mass versus charge state.

The relationship between sequence coverage and mass or charge state was further explored through linear regression analysis based on the scatter plots displayed in Figures S5 and S6. The resulting correlation R^2 values, slopes, and intercepts for each activation method are shown in Figure 2. The correlation R^2 values range from 0.05 to 0.5, relatively low values that suggest that there are many other factors that affect sequence coverage beyond just mass and charge state. The magnitude of the R^2 values suggests that charge state has a slightly greater impact than peptide mass on sequence coverage for HCD, whereas the peptide mass exerts a greater influence on sequence coverage than charge state for ETD, EThcD, and 213 nm UVPD. For 193 nm UVPD, the correlation is low for both charge state and mass, implying that the performance of 193 nm UVPD is not substantially influenced by either parameter. The slopes of the linear regressions are all negative, indicating that as peptide mass increases, the level of sequence coverage decreases. The magnitudes of the slopes are greatest for HCD, ETD, and EThcD, corresponding to a steeper drop in sequence coverage for larger peptides. The magnitude of the slope is the smallest for 193 nm UVPD, which in combination with the low correlation value indicates that mass and charge state have little relation to sequence coverage.

In order to rationalize the trends, the impact of the number of basic amino acids on the sequence coverage was considered as one influential factor on peptide fragmentation. As a simple approximation, the number of sites that are anticipated to sequester protons, making them immobile, was estimated based on the number of arginines in each peptide sequence. The known high basicity of arginine endows it with the greatest ability to sequester protons.[16] Two other amino acids with basic side-chains, lysine and histidine, have also been evaluated as potential proton-sequestering residues,[16] but their variable behavior and lower basicities compared to arginine obscured the discernment of significant impact in the present study. Consequently, the number of mobile protons was estimated by subtracting the number of arginines from the charge state of the peptide. The estimated number of potential mobile protons spanned zero (low charge stages and/or high number of arginines) to 7 (high charges states and/or low number of arginines). These estimations were also repeated by considering lysine or histidine residues as basic sites. Any mobile proton category containing less than 10 peptides was removed from further analysis owing to low population size, resulting in retention of only those categories corresponding to zero to five mobile protons (Tables S6−S8). Scatter plots of sequence coverage as a function of charge state (Figure S7) or peptide mass (Figure S8) were subjected to linear regression analysis for the peptides that fell into each of the six mobile proton categories (e.g., zero to five mobile protons based on charge state relative to the number of arginines). The resulting R^2 correlation values (Figure 3) and slopes (Figure 4) for each linear regression are shown for HCD, ETD, and 193 nm UVPD and for all activation methods in Figures S9−S17 (R^2, slopes, intercepts for the arginine, lysine, and histidine analysis). Correlation values for HCD are low when the number of mobile protons is zero but increase to R^2 values greater than 0.5 when the number of mobile protons is one to three, then gradually decrease for four or five mobile protons. This pattern supports previous outcomes described for tryptic peptides, in which the impact of mobile protons on the pathways of collisional activated dissociation has been broadly recognized.[36] The corresponding comparisons for EThcD and 193 nm UVPD do not show the same type of behavior as noted for HCD. Instead, the R^2 values and magnitudes of the slope steadily increase for EThcD, indicating a consistent positive correlation with number of mobile protons. There is no apparent pattern or correlation of mobile protons and sequence coverage for 193 nm UVPD.

Model Peptides. Four benchmark peptides, ranging from 3.0 to 4.3 kDa, were chosen to explore the trends observed in the middle-down digest in more depth. Each peptide has between 4 and 6 highly basic residues (Arg and Lys), which is another feature that differentiates them from typical tryptic peptides that contain a single Arg or Lys at the C-terminus (see Table 1). MS1 spectra of each of the four peptides are shown in Figure S18.

https://doi.org/10.1021/jasms.3c00405
J. Am. Soc. Mass Spectrom. 2024, 35, 1647−1656

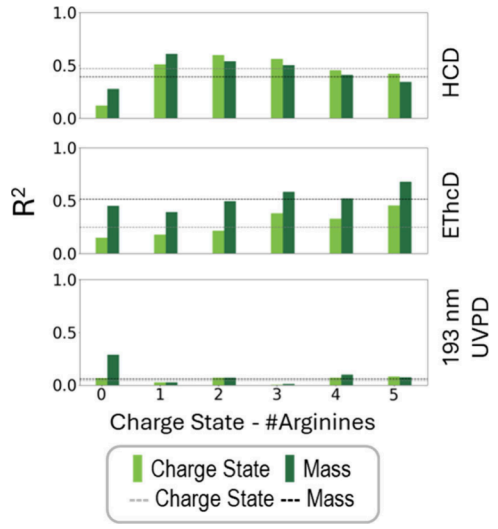

Figure 3. R^2 correlation values derived from linear regressions of sequence coverage vs peptide charge state or mass categorized based on the number of mobile protons defined as (charge state − number of arginines). The dark grey and light grey horizontal lines show the correlation of the combined data for sequence coverage vs. charge state and sequence coverage vs. mass, respectively.

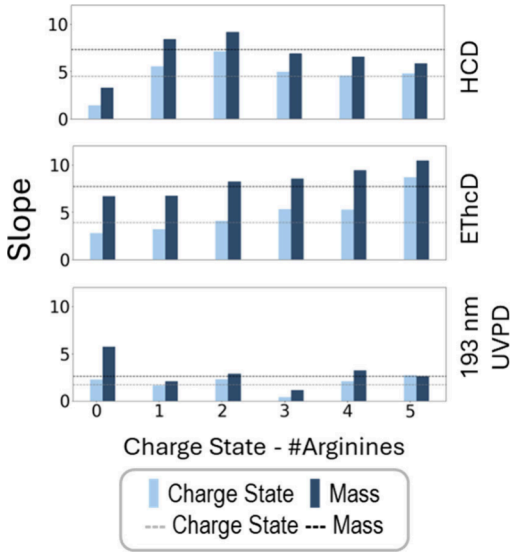

Figure 4. Slopes of linear regressions of sequence coverage vs charge state or peptide mass categorized based on the number of mobile protons defined as (charge stage − number of arginines). The dark grey and light grey horizontal lines show the slope of the combined data for sequence coverage vs. charge state and sequence coverage vs. mass, respectively.

Sequence Coverage. MS/MS spectra were collected for the three most abundant charge states of each of the four peptides. Examples of the resulting MS/MS spectra (HCD, ETD, EThcD, 213 nm UVPD, 193 nm UVPD) are shown for glucagon (4+) in Figures S19−23, and the identified fragment ions for all four peptides in three charge states using each of the five MS/MS methods are summarized in Tables S9−69. Sequence coverages are displayed in Figure 5. Trends for each ion activation method remained consistent for the set of the four peptides. The highest sequence coverage for HCD was achieved for the lowest charge state of each peptide, and sequence coverage decreased as the charge state increased, with the exception of neuromedin, which had a slightly lower sequence coverage for the 3+ charge state (88%) compared the 4+ charge state (96%). For example, the sequence coverage decreased from 88% (3+) to 41% (5+) for glucagon due to fragmentation occurring at an increasingly smaller region of the peptide at higher charge states. For ETD of neuromedin, glucagon and amyloid β, sequence coverage increased significantly with charge state, an outcome that reflects the well-known charge state dependence of electron-activation methods. The sequence coverage obtained by ETD increased from 20% (3+) to 92% (5+) for neuromedin and 13% (3+) to 94% (5+) for glucagon. Similar trends occur for EThcD; however, EThcD provides an overall sequence coverage boost compared to ETD often leading to sequence coverages over 90%. 193 nm UVPD, and 213 nm UVPD yielded consistently high sequence coverages, often 95% or greater, for all four peptides in all charge states.

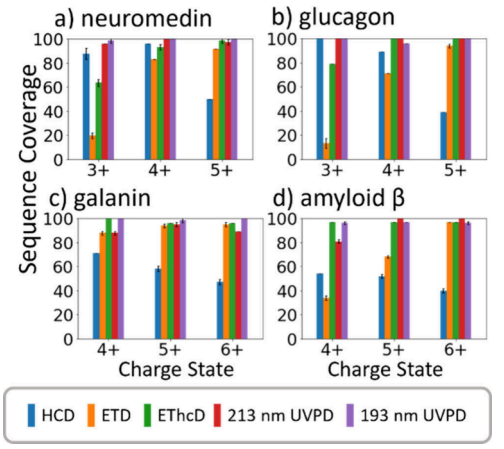

Figure 5. Sequence coverages of four large peptides: (a) neuromedin, (b) glucagon, (c) galanin, and (d) amyloid β using HCD, ETD, EThCD, 213 nm UVPD, and 193 nm UVPD.

Charge Site Analysis. Charge site analysis was undertaken to map the locations of protons of each peptide. For this method, the location of charge sites is estimated by monitoring the charge states of *a*/*x*-type fragment ions generated by 193 nm UVPD.[21] These fragment ions are postulated to originate directly by fast dissociation of the precursor ions in excited electronic states and are not charge-directed (e.g., not

Table 1. Sequences of Peptides with Corresponding Number of Prolines, Acidic, Aromatic, and Basic Residues, and Monoisotopic Mass

Peptide	Sequence	Number of P/DE/FWY/KRH	Monoisotopic Mass (Da)	Charge States
Neuromedin	FRVDEEFQSPFASQSRGYFLFRPRN	2/3/6/4 (0K 4R)	3078.52	3+, 4+, 5+
Glucagon	HSQGTFTSDYSKYLDSRRAQDFVQWLMNT	0/3/5/4 (1K 2R 1H)	3480.62	3+, 4+, 5+
Galanin	GWTLNSAGYLLGPHAIDNHRSFSDKHGLT	1/2/3/5 (1K 1R 3H)	3162.57	4+, 5+, 6+
Amyloid β	DAEFRHDSGYEVHHQKLVFFAEDVGSNKGAIIGLMVGGVV	0/6/4/6 (2K 1R 3H)	4327.15	4+, 5+, 6+

https://doi.org/10.1021/jasms.3c00405
J. Am. Soc. Mass Spectrom. 2024, 35, 1647−1656

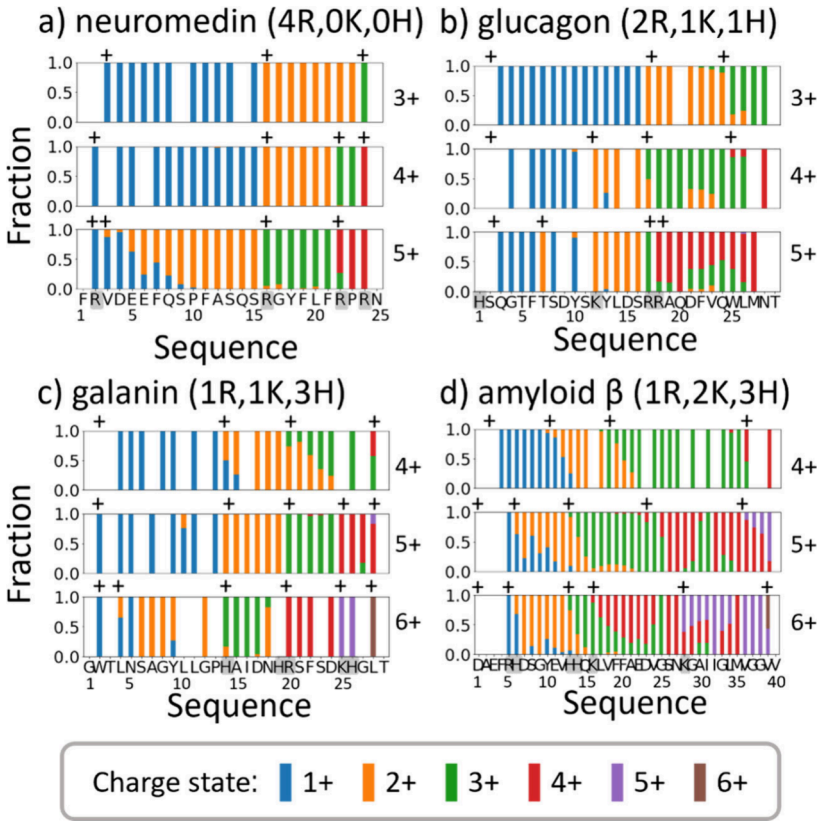

Figure 6. Charge state analysis based on the *a*-type fragment ions generated by 193 nm UVPD for (a) neuromedin, (b) glucagon, (c) galanin, and (d) amyloid *β*. Acidic residues are highlighted in gray in the sequence shown as the *x*-axis of each graph, and putative charge site locations are marked by plus signs above each graph.

mediated by mobile protons).[20] In particular, step changes in the charge states of the observed *a*-type fragment ions are used to demarcate the locations of each additional proton going from N-terminus to C-terminus (or from C-terminus to N-terminus for *x*-type fragment ions). The fraction of a specific a_n (or x_n) fragment ion in each charge state is mapped onto the peptide sequence based on the backbone cleavage site from which the fragment ion originates, as shown in Figure 6. For example, UVPD of the 3+ charge state of neuromedin results in the exclusive production of singly charged a_1 to a_{15} ions and then switches to doubly charged ions for a_{16} to a_{23}. This shift indications that there is an additional proton at a nearby residue. For the 5+ charge state of neuromedin, the shift between singly and doubly charged fragment ions is more gradual, with both charge states observed for a_3 to a_{11}. This "blurred" trend for the 5+ charge state of neuromedin suggests greater proton mobility, in contrast to the sequestration of protons at specific sites for the 3+ and 4+ charge states of the peptide. Examination of the charge states of the fragment ions generated by UVPD provides insight into the locations of the protons. Approximate locations of protons are indicated in Figure 6 as positive signs floated over the histograms of the fragment ion charge states.

The effect of basic sites on fragmentation pathways is shown by correlating charge site analysis to fragmentation efficiency curves. Fragmentation efficiency curves were generated for each peptide in each of the three charge states based on monitoring the summed fractional abundance of all fragment ions as a function of collision energy, as illustrated in Figure 7. The inflection points represent the energy required to dissociate the precursor to 50% of its original abundance. As expected, the fragmentation efficiency curves shift to the left for each peptide as a function of increasing charge state, indicating a lower onset for dissociation (e.g., lower $E_{1/2}$ value

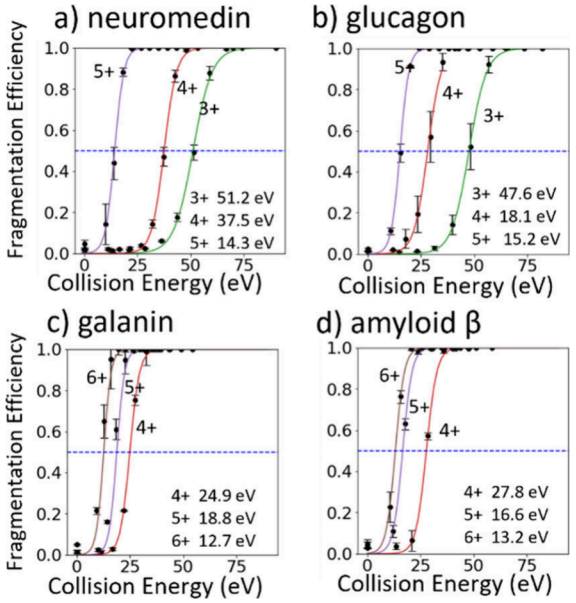

Figure 7. Fragmentation efficiency of each charge state was calculated based on the abundance of fragment ions relative to the abundances of all summed fragment ions plus precursor based on HCD (0 to 40 NCE corresponding to 0 to 80 eV) for three charge states of: (a) neuromedin, (b) glucagon, (c) galanin, and (d) amyloid *β*.

https://doi.org/10.1021/jasms.3c00405
J. Am. Soc. Mass Spectrom. 2024, 35, 1647−1656

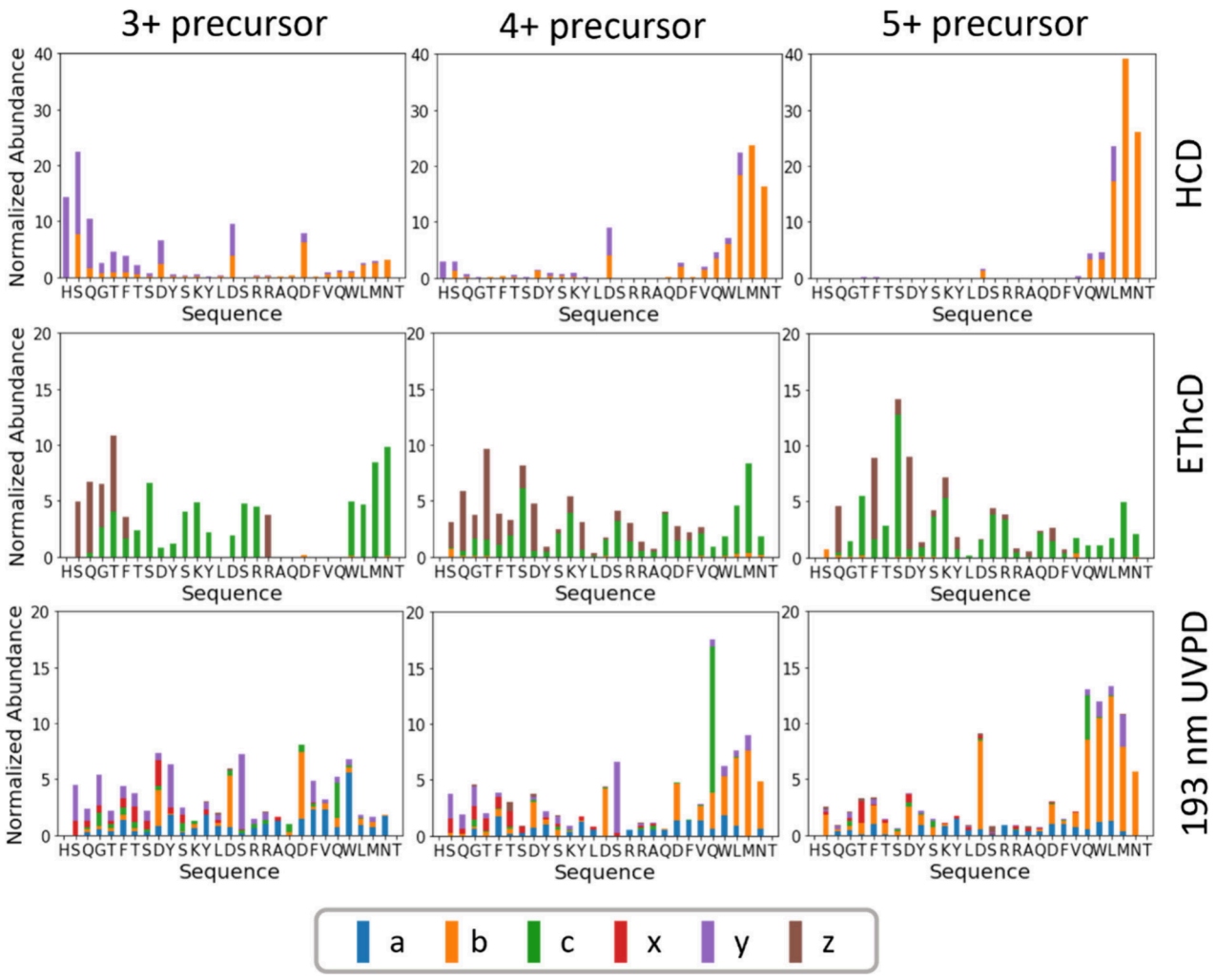

Figure 8. Fragment abundance maps of the 3+, 4+, and 5+ charge states of glucagon using HCD, EThcD, and 193 nm UVPD.

as precursor charge state increases). This uniform trend aligns with the mobile proton model for collision induced dissociation of peptides; the availability of a greater number of mobile protons decreases the energy required for fragmentation because the protons are not exclusively sequestered at basic sites.[16]

The trends in the $E_{1/2}$ values were evaluated in tandem with the charge site analysis derived from the UVPD spectra for each of the four peptides. Charge site analysis can also be done using *x*-type fragment ions (Figure S24) for 193 nm UVPD, but the less complete series of *x*-ions results in gaps in the charge site information. This type of charge site analysis may also be undertaken using 213 nm UVPD (see Figures S25 and S26), yielding similar trends as observed for 193 nm UVPD.

Neuromedin yields similar charge site locations for three of the protons for the 3+ and 4+ precursors (Arg2, Arg15, and Arg23), with an additional charge site at Arg21 for the 4+ precursor (Figure 6a). Based on the sharp transitions in the charge states of the fragment ions, there are no mobile protons, and this outcome is similarly reflected in the fragmentation efficiencies curves (Figure 7a). For the 5+ charge state of neuromedin, a gradual shift in charge state from Val3 to Pro11 fragment ions indicates proton mobility, also in agreement with the fragmentation efficiency curve that shifts to the left and results in a much lower $E_{1/2}$ value (Figure 6a, Figure 7a).

Glucagon has two arginines (Arg17 and Arg18); however, since they are adjacent, only Arg 17 acts as a charge site for the 3+ and 4+ charge states. The first charge site is located at the N-terminus, with additional charge sites at Arg17 for the 3+ peptide and Lys 12 for the 4+ and 5+ peptide. Additionally, there is evidence that protons may be located at the two adjacent Arg sites (Arg 17, Arg18) for the 5+ charge state. The charge state transitions observed for the fragment ions of all three charge states of glucagon are suggestive of mobile proton behavior (Figure 6b). The 5+ and 6+ charge states of galanin have similar charge site locations (the N-terminus, His14, Arg20, Lys20). Interestingly, while the somewhat blurred charge state transitions for the fragment ions of the 4+ charge state are suggestive of two mobile protons, there is limited or no evidence for a mobile proton for the 5+ charge state (Figure 6c). Amyloid β only has one arginine, Arg5, and the charge site analysis for this peptide indicates that most of the protons are mobile based on the very blurred charge state transitions for the fragment ions (Figure 6d). This results in lower $E_{1/2}$ values for fragmentation for all three charge states of the peptide, the lowest values and most narrow range of energies among the four peptides (Figure 6d).

Backbone Cleavage Maps. Backbone cleavage maps were generated for three charge states of each peptide based on each ion activation method. These maps display the abundances of

https://doi.org/10.1021/jasms.3c00405
J. Am. Soc. Mass Spectrom. 2024, 35, 1647−1656

fragment ions according to the backbone cleavage position from which they originated, as displayed in Figure 8 for HCD, EThcD, and 193 nm UVPD for glucagon and S27−30 for neuromedin, glucagon, galanin, and amyloid β, respectively, for all five activation methods. The maps offer a means to visualize the pattern of backbone cleavages for each peptide and showcase highly preferred "cut" sites, such as the prominent cleavages at Asp9, Asp15, and Asp21 upon HCD of the 3+ charge state of glucagon in Figure 8.

The cleavage maps produced by HCD indicate that backbone cleavages are often clustered around one section of each peptide, often narrowing as the charge state of the peptide increases. This trend explains the decreasing sequence coverage observed for each peptide as the charge stage increases. There are no apparent sequence motifs or specific amino acids that drive this clustered fragmentation behavior, and although there is some degree of preferential cleavage related to acidic residues (i.e., Figure S27a, maps for neuromedin), in general, preferential cleavages are not dominant.

Both EThcD and 193 nm UVPD result in more uniform backbone cleavage maps for all four peptides in each of the charge states, consistent with the high sequence coverages noted earlier. ETD and EThcD yield similar backbone cleavage maps for the higher charge states, with the most notable differences occurring at low charge states for which ETD often results in low sequence coverage. The dependence of ETD on charge density is well-known and is exemplified by the very sparce maps generated upon ETD of the 3+ charge state of neuromedin and glucagon (Figure S27−28) and the 4+ charge states of galanin and amyloid β (Figure S29−30). Both 193 nm UVPD and 213 nm UVPD exhibit the broadest array of backbone cleavage sites and produce the largest diversity of fragment ion types. Notable differences between 193 nm UVPD and 213 nm UVPD include the enhancement of relative abundances of b/y fragment ions for 193 nm UVPD, especially for glucagon and amyloid β (Figure S28 and S30).

The lack of variation and consistently high sequence coverages for UVPD as a function of charge state indicate that UVPD does not depend greatly on the availability of mobile protons. However, the backbone cleavage maps show that b/y type ions are more dominant for UVPD of higher precursor charge states and the fragmentation patterns begin to increasingly resemble those generated by HCD. This outcome likely reflects the two distinct fragmentation mechanisms for UVPD: (i) direct dissociation from excited states, which is not a charge state dependent process and which accounts for prevalent but low abundance a/x ions generated from cleavage at virtually every backbone position, and (ii) internal conversion with intramolecular vibrational energy redistribution (IVR), which produces b/y ions akin to collision induced dissociation and which becomes more prominent for the higher charge states.[20] UVPD of all four peptides yield higher abundance b/y ions for higher charge states.

Fragmentation efficiency values listed on the fragment abundance maps in Figure S27−30 show that fragmentation efficiency generally increases with charge state. For example, for glucagon (Figure S28) the fragmentation efficiencies increase from 49% to 89% for EThcD and 31% to 79% for 193 nm for the 3+ and 5+ charge states, respectively.

Preferential Cleavages. The distributions of fragment ions were also categorized based on whether they originate from preferential cleavages (N-terminal to proline, C-terminal to aspartic and glutamic acid, and cleavages adjacent to aromatic residues) or nonspecific cleavages (all other backbone cleavages) (Figure 9). Cleavages occurring N-terminal to proline are one type of preferential cleavage commonly observed upon collisional activation, attributed to the basicity of the nitrogen of the proline residue allowing capture of a mobile proton.[37] Glucagon and amyloid β both lacked prolines, and the proline effect was minimal or not observed for the other two peptides for ETD and EThcD. Fragment ions originating from cleavages N-terminal to proline were notably enhanced for HCD and both 193 and 213 nm UVPD for neuromedin. Backbone cleavages C-terminal to aspartic and glutamic acid are often preferential upon collisional activation of peptides in low charge states because the lack of mobile protons allows the hydrogens of carboxylate groups to participate in fragmentation.[16] This type of cleavage was enhanced for the 3+ and 4+ charge states of neuromedin and glucagon for HCD but was not observed at all for galanin and amyloid β. Some C-terminal acidic cleavages were observed upon EThcD and UVPD but were not unusually prevalent nor correlated strongly with the precursor charge state. The presence of aromatic amino acids, phenylalanine, tyrosine and tryptophan, is known to enhance fragmentation efficiency upon both 193 and 213 nm UVPD.[38,39] This impact of aromatic amino acids is not charge-state dependent, and it is the most consistently enhanced type of preferential cleavage observed for all of the peptides for all activation methods.

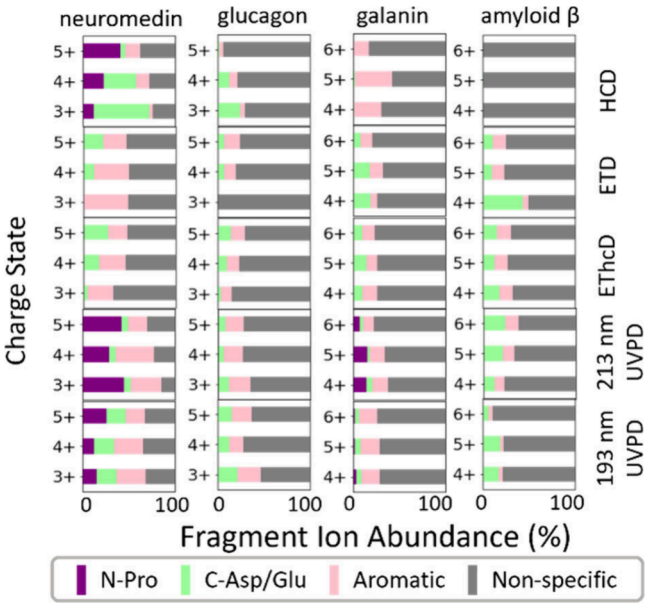

Figure 9. Percentages of fragment ion current originating from preferential cleavages (N-terminal to proline, C-terminal to aspartic and glutamic acid, and cleavages adjacent to aromatic residues) for each peptide for each activation method.

CONCLUSIONS

In this work, fragmentation trends for HCD, ETD, EThcD, 193 nm UVPD and 213 nm UVPD were compared for larger middle-down sized peptides. Trends were investigated for a set of peptides generated from limited GluC digestion of *E. coli* ribosomal proteins. Linear regression analysis was used to examine the relationship between charge state and mass to sequence coverage, with HCD, ETD and EThcD having the

https://doi.org/10.1021/jasms.3c00405
J. Am. Soc. Mass Spectrom. 2024, 35, 1647−1656

highest correlation coefficients. Both 213 and 193 nm UVPD had lower correlation coefficients, with 193 nm UVPD in particular showing that sequence coverage had little dependence on charge state and mass. Results considering both the sequence coverage and Proteome Discoverer score show that although UVPD identified fewer peptides compared to EThcD, UVPD afforded higher sequence coverages and higher confidence peptide identifications for larger peptides, specifically those in the 4−10 kDa range. Analysis of four large model peptides showed that sequence coverages for HCD, ETD and EThcD are charge state dependent. Although sequence coverages for UVPD remain highly independent of charge state, there were changes in fragment ion abundances with sequence coverage, particularly increases in abundances of *b*/*y* ions for peptides in the higher charge states. Charge site analysis was used to determine the location of mobile and sequestered protons. In combination with the fragmentation efficiency curves, the trends show that the energy required for fragmentation depends on the size and charge state of the peptide as well as the number of basic residues. Preferential cleavages N-terminal to prolines for UVPD and preferential cleavages C-terminal to acidic residues (observed for all activation methods), are common, with a more notable charge state dependence specifically for HCD.

The focus of this fundamental study was aimed at developing a better understanding of the factors, particularly peptide size and basic sites, that mediate the success of deriving sequence information from large peptides. The wide range of MS/MS methods now widely available on many mass spectrometers provide many new opportunities for expanding the scope of middle-down proteomics strategies that remain unexplored.

■ ASSOCIATED CONTENT

Data Availability Statement

Identified fragment ions from all charge states of 4 model peptides, using all 5 activation methods, and Proteome Discoverer results are available via MSV000093440 at the MassIVE repository: https://massive.ucsd.edu/ProteoSAFe/dataset.jsp?task=e9ae58d5ca1d40649e0b334d82c40cd0.

Supporting Information

The Supporting Information is available free of charge at https://pubs.acs.org/doi/10.1021/jasms.3c00405.

Middle-down digest chromatogram; identified peptides, sequence coverage, and Proteome Discoverer scores of middle-down digest by peptide mass and charge, MS1 and MS/MS spectra of 4 model peptides, charge site analysis with a-type and x-type fragment ions using 193 and 213 nm UVPD, fragment ion abundance maps of 4 model peptides (PDF)

Tables S1−5. Proteome Discoverer analysis of Glu-C digest of E. coli ribosomal proteins (XLSX)

Tables S9−69. List of identified fragment ions for neuromedin, glucagon, galanin, and amyloid β (XLSX)

■ AUTHOR INFORMATION

Corresponding Author

Jennifer S. Brodbelt − *Department of Chemistry, The University of Texas at Austin, Austin, Texas 78712, United States;* orcid.org/0000-0003-3207-0217; Email: jbrodbelt@cm.utexas.edu

Author

Jessica Hellinger − *Department of Chemistry, The University of Texas at Austin, Austin, Texas 78712, United States*

Complete contact information is available at: https://pubs.acs.org/10.1021/jasms.3c00405

Notes

The authors declare no competing financial interest.

■ ACKNOWLEDGMENTS

We acknowledge the following funding sources: NSF (Grant CHE-2203602) and the Welch Foundation (Grant F-1155). The assistance of Kerri West is gratefully acknowledged.

■ REFERENCES

(1) Schaffer, L. V.; Millikin, R. J.; Miller, R. M.; Anderson, L. C.; Fellers, R. T.; Ge, Y.; Kelleher, N. L.; LeDuc, R. D.; Liu, X.; Payne, S. H.; Sun, L.; Thomas, P. M.; Tucholski, T.; Wang, Z.; Wu, S.; Wu, Z.; Yu, D.; Shortreed, M. R.; Smith, L. M. Identification and Quantification of Proteoforms by Mass Spectrometry. *PROTEOMICS* **2019**, *19* (10), 1800361.

(2) Pandeswari, P. B.; Sabareesh, V. Middle-down Approach: A Choice to Sequence and Characterize Proteins/Proteomes by Mass Spectrometry. *RSC Adv.* **2019**, *9* (1), 313−344.

(3) Cristobal, A.; Marino, F.; Post, H.; van den Toorn, H. W. P.; Mohammed, S.; Heck, A. J. R. Toward an Optimized Workflow for Middle-Down Proteomics. *Anal. Chem.* **2017**, *89* (6), 3318−3325.

(4) Wu, C.; Tran, J. C.; Zamdborg, L.; Durbin, K. R.; Li, M.; Ahlf, D. R.; Early, B. P.; Thomas, P. M.; Sweedler, J. V.; Kelleher, N. L. A Protease for "middle-down" Proteomics. *Nat. Methods* **2012**, *9* (8), 822−824.

(5) Golghalyani, V.; Neupärtl, M.; Wittig, I.; Bahr, U.; Karas, M. ArgC-Like Digestion: Complementary or Alternative to Tryptic Digestion? *J. Proteome Res.* **2017**, *16* (2), 978−987.

(6) Giansanti, P.; Tsiatsiani, L.; Low, T. Y.; Heck, A. J. R. Six Alternative Proteases for Mass Spectrometry-Based Proteomics beyond Trypsin. *Nat. Protoc* **2016**, *11* (5), 993−1006.

(7) Srzentić, K.; Zhurov, K. O.; Lobas, A. A.; Nikitin, G.; Fornelli, L.; Gorshkov, M. V.; Tsybin, Y. O. Chemical-Mediated Digestion: An Alternative Realm for Middle-down Proteomics? *J. Proteome Res.* **2018**, *17* (6), 2005−2016.

(8) Watts, E.; Williams, J. D.; Miesbauer, L. J.; Bruncko, M.; Brodbelt, J. S. Comprehensive Middle-Down Mass Spectrometry Characterization of an Antibody-Drug Conjugate by Combined Ion Activation Methods. *Anal. Chem.* **2020**, *92* (14), 9790−9798.

(9) An, Y.; Zhang, Y.; Mueller, H.-M.; Shameem, M.; Chen, X. A New Tool for Monoclonal Antibody Analysis. *mAbs* **2014**, *6* (4), 879−893.

(10) Fornelli, L.; Ayoub, D.; Aizikov, K.; Beck, A.; Tsybin, Y. O. Middle-Down Analysis of Monoclonal Antibodies with Electron Transfer Dissociation Orbitrap Fourier Transform Mass Spectrometry. *Anal. Chem.* **2014**, *86* (6), 3005−3012.

(11) Young, N. L.; Plazas-Mayorca, M. D.; Garcia, B. A. Systems-Wide Proteomic Characterization of Combinatorial Post-Translational Modification Patterns. *Expert Review of Proteomics* **2010**, *7* (1), 79−92.

(12) Sidoli, S.; Garcia, B. A. Middle-Down Proteomics: A Still Unexploited Resource for Chromatin Biology. *Expert Rev. Proteomics* **2017**, *14* (7), 617−626.

(13) Malinovska, L.; Cappelletti, V.; Kohler, D.; Piazza, I.; Tsai, T.-H.; Pepelnjak, M.; Stalder, P.; Dörig, C.; Sesterhenn, F.; Elsässer, F.; Kralickova, L.; Beaton, N.; Reiter, L.; de Souza, N.; Vitek, O.; Picotti, P. Proteome-Wide Structural Changes Measured with Limited Proteolysis-Mass Spectrometry: An Advanced Protocol for High-Throughput Applications. *Nat. Protoc* **2023**, *18* (3), 659−682.

(14) Leutert, M.; Entwisle, S. W.; Villén, J. Decoding Post-Translational Modification Crosstalk With Proteomics. *Molecular & Cellular Proteomics* **2021**, *20*, 100129.
(15) Melby, J. A.; Roberts, D. S.; Larson, E. J.; Brown, K. A.; Bayne, E. F.; Jin, S.; Ge, Y. Novel Strategies to Address the Challenges in Top-Down Proteomics. *J. Am. Soc. Mass Spectrom.* **2021**, *32* (6), 1278−1294.
(16) Wysocki, V. H.; Tsaprailis, G.; Smith, L. L.; Breci, L. A. Mobile and Localized Protons: A Framework for Understanding Peptide Dissociation. *Journal of Mass Spectrometry* **2000**, *35* (12), 1399−1406.
(17) Dongré, A. R.; Jones, J. L.; Somogyi, Á.; Wysocki, V. H. Influence of Peptide Composition, Gas-Phase Basicity, and Chemical Modification on Fragmentation Efficiency: Evidence for the Mobile Proton Model. *J. Am. Chem. Soc.* **1996**, *118* (35), 8365−8374.
(18) Liu, J.; McLuckey, S. A. Electron Transfer Dissociation: Effects of Cation Charge State on Product Partitioning in Ion/Ion Electron Transfer to Multiply Protonated Polypeptides. *Int. J. Mass Spectrom.* **2012**, *330*−*332*, 174−181.
(19) Brodbelt, J.; Morrison, L.; Santos, I. Ultraviolet Photodissociation Mass Spectrometry for Analysis of Biological Molecules. *Chem. Rev.* **2020**, *120* (7), 3328−3380.
(20) Julian, R. The Mechanism behind Top-Down UVPD Experiments: Making Sense of Apparent Contradictions. *J. Am. Soc. Mass Spectrom.* **2017**, *28* (9), 1823−1826.
(21) Morrison, L. J.; Brodbelt, J. S. Charge Site Assignment in Native Proteins by Ultraviolet Photodissociation (UVPD) Mass Spectrometry. *Analyst* **2016**, *141* (1), 166−176.
(22) Bashyal, A.; Sanders, J. D.; Holden, D. D.; Brodbelt, J. S. Top-Down Analysis of Proteins in Low Charge States. *J. Am. Soc. Mass Spectrom.* **2019**, *30* (4), 704−717.
(23) Sipe, S. N.; Brodbelt, J. S. Impact of Charge State on 193 Nm Ultraviolet Photodissociation of Protein Complexes. *Phys. Chem. Chem. Phys.* **2019**, *21* (18), 9265−9276.
(24) Zhou, M.; Liu, W.; Shaw, J. B. Charge Movement and Structural Changes in the Gas-Phase Unfolding of Multimeric Protein Complexes Captured by Native Top-Down Mass Spectrometry. *Anal. Chem.* **2020**, *92* (2), 1788−1795.
(25) Hoshino, A.; Kim, H. S.; Bojmar, L.; Gyan, K. E.; Cioffi, M.; Hernandez, J.; Zambirinis, C. P.; Rodrigues, G.; Molina, H.; Heissel, S.; Mark, M. T.; Steiner, L.; Benito-Martin, A.; Lucotti, S.; Di Giannatale, A.; Offer, K.; Nakajima, M.; Williams, C.; Nogués, L.; Pelissier Vatter, F. A.; Hashimoto, A.; Davies, A. E.; Freitas, D.; Kenific, C. M.; Ararso, Y.; Buehring, W.; Lauritzen, P.; Ogitani, Y.; Sugiura, K.; Takahashi, N.; Alečković, M.; Bailey, K. A.; Jolissant, J. S.; Wang, H.; Harris, A.; Schaeffer, L. M.; García-Santos, G.; Posner, Z.; Balachandran, V. P.; Khakoo, Y.; Raju, G. P.; Scherz, A.; Sagi, I.; Scherz-Shouval, R.; Yarden, Y.; Oren, M.; Malladi, M.; Petriccione, M.; De Braganca, K. C.; Donzelli, M.; Fischer, C.; Vitolano, S.; Wright, G. P.; Ganshaw, L.; Marrano, M.; Ahmed, A.; DeStefano, J.; Danzer, E.; Roehrl, M. H. A.; Lacayo, N. J.; Vincent, T. C.; Weiser, M. R.; Brady, M. S.; Meyers, P. A.; Wexler, L. H.; Ambati, S. R.; Chou, A. J.; Slotkin, E. K.; Modak, S.; Roberts, S. S.; Basu, E. M.; Diolaiti, D.; Krantz, B. A.; Cardoso, F.; Simpson, A. L.; Berger, M.; Rudin, C. M.; Simeone, D. M.; Jain, M.; Ghajar, C. M.; Batra, S. K.; Stanger, B. Z.; Bui, J.; Brown, K. A.; Rajasekhar, V. K.; Healey, J. H.; de Sousa, M.; Kramer, K.; Sheth, S.; Baisch, J.; Pascual, V.; Heaton, T. E.; La Quaglia, M. P.; Pisapia, D. J.; Schwartz, R.; Zhang, H.; Liu, Y.; Shukla, A.; Blavier, L.; DeClerck, Y. A.; LaBarge, M.; Bissell, M. J.; Caffrey, T. C.; Grandgenett, P. M.; Hollingsworth, M. A.; Bromberg, J.; Costa-Silva, B.; Peinado, H.; Kang, Y.; Garcia, B. A.; O'Reilly, E. M.; Kelsen, D.; Trippett, T. M.; Jones, D. R.; Matei, I. R.; Jarnagin, W. R.; Lyden, D. Extracellular Vesicle and Particle Biomarkers Define Multiple Human Cancers. *Cell* **2020**, *182* (4), 1044−1061.
(26) Kalli, A.; Håkansson, K. Electron Capture Dissociation of Highly Charged Proteolytic Peptides from Lys N, Lys C and Glu C Digestion. *Mol. BioSyst.* **2010**, *6* (9), 1668−1681.
(27) Sweredoski, M. J.; Moradian, A.; Raedle, M.; Franco, C.; Hess, S. High Resolution Parallel Reaction Monitoring with Electron Transfer Dissociation for Middle-down Proteomics. *Analytical chemistry* **2015**, *87* (16), 8360−8366.
(28) Cotham, V. C.; Horton, A. P.; Lee, J.; Georgiou, G.; Brodbelt, J. S. Middle-Down 193-Nm Ultraviolet Photodissociation for Unambiguous Antibody Identification and Its Implications for Immunoproteomic Analysis. *Anal. Chem.* **2017**, *89* (12), 6498−6504.
(29) Sanders, J. D.; Greer, S. M.; Brodbelt, J. S. Integrating Carbamylation and Ultraviolet Photodissociation Mass Spectrometry for Middle-Down Proteomics. *Anal. Chem.* **2017**, *89* (21), 11772−11778.
(30) Fornelli, L.; Srzentić, K.; Huguet, R.; Mullen, C.; Sharma, S.; Zabrouskov, V.; Fellers, R. T.; Durbin, K. R.; Compton, P. D.; Kelleher, N. L. Accurate Sequence Analysis of a Monoclonal Antibody by Top-Down and Middle-Down Orbitrap Mass Spectrometry Applying Multiple Ion Activation Techniques. *Anal. Chem.* **2018**, *90* (14), 8421−8429.
(31) Kundinger, S. R.; Bishof, I.; Dammer, E. B.; Duong, D. M.; Seyfried, N. T. Middle-Down Proteomics Reveals Dense Sites of Methylation and Phosphorylation in Arginine-Rich RNA-Binding Proteins. *J. Proteome Res.* **2020**, *19* (4), 1574−1591.
(32) Greer, S. M.; Sidoli, S.; Coradin, M.; Schack Jespersen, M.; Schwämmle, V.; Jensen, O. N.; Garcia, B. A.; Brodbelt, J. S. Extensive Characterization of Heavily Modified Histone Tails by 193 Nm Ultraviolet Photodissociation Mass Spectrometry via a Middle-Down Strategy. *Anal. Chem.* **2018**, *90* (17), 10425−10433.
(33) Klein, D. R.; Holden, D. D.; Brodbelt, J. S. Shotgun Analysis of Rough-Type Lipopolysaccharides Using Ultraviolet Photodissociation Mass Spectrometry. *Anal. Chem.* **2016**, *88* (1), 1044−1051.
(34) Juetten, K. J.; Brodbelt, J. S. MS-TAFI: A Tool for the Analysis of Fragment Ions Generated from Intact Proteins. *J. Proteome Res.* **2023**, *22* (2), 546−550.
(35) Rosenberg, J.; Parker, W. R.; Cammarata, M. B.; Brodbelt, J. S. UV-POSIT: Web-Based Tools for Rapid and Facile Structural Interpretation of Ultraviolet Photodissociation (UVPD) Mass Spectra. *J. Am. Soc. Mass Spectrom.* **2018**, *29* (6), 1323−1326.
(36) Paizs, B.; Suhai, S. Fragmentation Pathways of Protonated Peptides. *Mass Spectrom. Rev.* **2005**, *24* (4), 508−548.
(37) Raulfs, M. D. M.; Breci, L.; Bernier, M.; Hamdy, O. M.; Janiga, A.; Wysocki, V.; Poutsma, J. C. Investigations of the Mechanism of the "Proline Effect" in Tandem Mass Spectrometry Experiments: The "Pipecolic Acid Effect. *J. Am. Soc. Mass Spectrom.* **2014**, *25* (10), 1705−1715.
(38) Madsen, J. A.; Boutz, D. R.; Brodbelt, J. S. Ultrafast Ultraviolet Photodissociation at 193 Nm and Its Applicability to Proteomic Workflows. *J. Proteome Res.* **2010**, *9* (8), 4205−4214.
(39) Kolbowski, L.; Belsom, A.; Rappsilber, J. Ultraviolet Photodissociation of Tryptic Peptide Backbones at 213 Nm. *J. Am. Soc. Mass Spectrom.* **2020**, *31* (6), 1282−1290.

https://doi.org/10.1021/jasms.3c00405
J. Am. Soc. Mass Spectrom. 2024, 35, 1647−1656